Functionalized MXene Nanosheets and Al-Doped ZnO Nanoparticles for Flexible Transparent Electrodes

Nag Riya, Layek Rama Kanta, Bera Abhijit

DOI: 10.1021/acsanm.2c03916

Functionalized MXene Nanosheets and Al-Doped ZnO Nanoparticles for Flexible Transparent Electrodes

*Riya Nag, Rama Kanta Layek, and Abhijit Bera**

Department of Physics, Midnapore College (Autonomous), Raja Bazar Main Rd, 721101 Midnapore, W.B., India
School of Engineering Science, Department of Separation Science, LUT University, Mukkulankatu 19, FI-15210 Lahti, Finland

Email: abhijit.bera@midnaporecollege.ac.in

ABSTRACT: Transparent, flexible, and chemically stable conducting electrodes are the most important key component for fabricating optoelectronic devices. However, in conventional bulk metal-semiconductor (MS) junction Fermi-level pinning is a major concern that limits the charge transport properties of the devices. In this work, we have designed MS junctions using two-dimensional (2D) MXene nanosheets and Al-doped ZnO nanoparticles as a metal and an n-type semiconductor, respectively. The heterojunction was formed by layer-by-layer self-assembly on an ITO substrate and probed by Pt/Ir STM tip at room temperature. By recording the tunneling current of the components that in turn yielded the density of states of the materials, we could identify their energy positions to determine the band alignments. We then proceeded to form heterojunctions and characterized their current-voltage characteristics through scanning tunneling spectroscopy. The junctions showed rectification and the rectification ratio varied with the semiconductor doping concentrations. However, the shift of the Fermi level towards the conduction band edge of the semiconductor reduces the Schottky barrier width and consequently lowers the rectification ratio. Additionally, the MS junction with the polyallylamine (PAH) functionalized MXene nanosheets and the ZnO layer show a non-rectifying nature with low contact resistance at the interface. This work shows how a functionalized 2D-metal MXene and doped ZnO nanoparticle can tune the MS junction properties, used for implementing various flexible optoelectronic devices and transistor applications.

KEYWORDS: MXene nanosheets; metal-semiconductor junction; transparent electrode; layer-by-layer self-assembly; Fermi level pinning; scanning tunneling spectroscopy

1. INTRODUCTION:

Highly transparent, conductive, and chemically stable electrodes are crucial factors for achieving high efficiency in photovoltaic and transistor devices.[1-5] The high transparency of the electrodes allows more photons to be harvested, thus leading to increased absorption. The excellent electrical conductivity, high optical transmittance, large chemical stability, low cost, and suitable band alignment of titanium-based MXenes make them ideal candidates for transparent electrodes.[6-9] The outstanding mechanical strength of MXene also provides an opportunity to apply it as a flexible electrode in wearable electronic devices.[10-12]

When a metal is in contact with a semiconductor, a Schottky barrier may form due to the misalignment between the metal work function and the electron or hole affinity of the semiconductor. This Schottky barrier creates high contact resistance at the junction and restricts current in only one direction.[13-16] Theoretically, an Ohmic contact can be possible to achieve at the MS junction if the metal work functions are aligned with the conduction or valence band edges of the semiconductors. But in practice, metals form Schottky contacts irrespective of work function since the Fermi level of metal is pinned at a certain energy level at the semiconductor interface.[17-20] This Fermi-level pinning arises from the surface states of the semiconductor. Thus, we need new and approachable routes to achieve an ideal MS junction where the metal's work function aligns with the conduction or valence band of the semiconductor without Fermi-level pinning.[21-25] By introducing a graphene layer in between the MS-junction, the Schottky properties can be altered to Ohmic and reduce the Fermi level pinning of the semiconductor.[26-28] The graphene layer also modulates its work function via doping of metal impurities which reduces the Schottky height and facilitates charge transport in both directions.[28, 29] The work function of graphene can also be modified by the functionalization of some chemical elements.[30]

The choice of an appropriate charge transport layer (CTL) is exceptionally important for securing high performance in photovoltaic cells. In both conventional and inverted structures, a photoactive layer is inserted between the indium tin oxide (ITO) electrode and/or metal electrode.[31-34] These CTLs are either a hole transport layer (HTL) or an electron transport layer (ETL), according to their functionalities, and are employed to adjust the photoactive layer/electrode interfaces.[35-40] These CTLs perform various important functions, such as tuning the polarity of the electrodes (hole-collecting or electron-collecting), adjusting the energy barriers between the photoactive layer and the electrodes for efficient charge carrier transportation, preventing oxygen and moisture from penetrating the photoactive layer, and finally choosing one type of charge carrier and reducing charge carrier recombination. The

excellent conductivity, high optical transmittance, tunable work function, and outstanding mobility of MXenes make them promising candidates for interfacial materials.[41-44]

In a fresh MXene layer, the Fermi energy coincides with the conical points when treated with other chemicals or doped with an impurity it can significantly change its electronic properties. The work function of MXene can be increased by a UV ozone treatment and decreased through treatment with hydrazine by the oxidation and reduction of MXene, respectively. It can be thus tuned in a range from 4.08 to 5.33 eV.[45-47] The tunable work function MXene was used to design various photovoltaic cells with Ti_3C_2-based ETLs and HTLs, respectively.[45, 48] A similar phenomenon was observed in the amine (NH_2) functionalized self-assembled monolayer of graphene where the work function of graphene was reduced due to the n-doping by amine.[49]

In this work, we have formed an MS junction by inserting the MXene layer between the ITO and ZnO nanoparticles monolayer and probed the heterojunction by STM tip through scanning tunnelling spectroscopy. The junction was formed by a layer-by-layer approach by specific functionalization of individual materials. The insertion of MXene not only prevents Fermi-level pinning at the ITO-ZnO junction it also modulates the work function of the substrate to monitor the conduction or valence band edges of the semiconductor. The functionalized MXene can reduce or even potentially eliminate the Schottky barrier at the MS junction by reducing its work function. Thus, we were able to tune the work function of MXene and the Al-doped ZnO nanoparticles to form a low-resistance channel that can be used as an efficient flexible transparent electrode in optoelectronic devices.

2. EXPERIMENTAL SECTION:

Materials:

AR grade reagents of titanium aluminium carbide powder (>99%) were purchased from Nanoshel, lithium fluoride (300 mesh), poly-allylamine hydrochloride (PAH, average M_w~17,500) were purchased from Sigma Aldrich, zinc acetate dihydrate (>98%), aluminium nitrate (>98%), potassium hydroxide were purchased from Merck and used without further purification, DI water was prepared from MilliQ Millipore ultrapure water purification system.

Synthesis of MXene:

Single and multilayer MXenes were grown through reported synthesis routes by etching the Al from the Max phase (Ti_3AlC_2).[50] To do so, 0.3 g lithium fluoride (LiF) was added to a 6 M 6 mL HCl solution in a Teflon-coated beaker. The mixture was allowed to stir for 15 min to get the perfectly dissolved etching solution. Then 0.3 g max phase powder was slowly added to the solution and placed in an ice bath to minimize overheating. The final mixture was then

agitated (500 rpm) for 24 hours at 35ºC. After completing the etching process DI water was added to the suspension for centrifugation and poured out the supernatant until a neutral pH was reached. At this stage, DI water was added to the sediment and centrifuged for 1 hour at 3500 rpm. Therefore, the dark green supernatant containing large flake MXenes was collected and stored in the refrigerator for further use.

To functionalize the MXene with poly-allylamine hydrochloride (PAH, M_w=17,500), a 0.03 mM 20 mL aqueous PAH solution was prepared in a beaker. A 0.5 ml MXene (4 mg/ml) was then added to this solution and continuously stirred for 45 mins with a speed of 550 rpm. After functionalization, the solution was centrifuged multiple times with water at 6000 rpm to remove excess and loosely attached PAH from the MXene surface. The sediment was then collected and dissolved in 20 mL water for further use in LBL as an electrophilic ($-CH_3^+$) moiety at the surface.

Synthesis of Al-doped ZnO nanoparticle:

For the growth of ZnO nanoparticles, we have followed a reported route.[51] We prepared two separate solutions of zinc acetate dihydrate, $Zn(CH_3COO)_2.2H_2O$ and potassium hydroxide, KOH in methanol. 13.4 mmol of zinc acetate dihydrate with 63 ml methanol and 23 mmol potassium hydroxide with 33 ml methanol were taken in a beaker and two solutions were sonicated for 30 min. Zinc acetate solution was stirred with a magnetic stirrer at 60ºC and the potassium hydroxide solution was added to the stirred solution by a slow dropwise process. The transparent solution was then gradually turned into a white precipitated solution. The container was heated under the same conditions for another 30 min. After cooling to room temperature, the supernatant was decanted and the precipitate was washed twice with methanol. Finally, the precipitate was dispersed in deionized water to prepare the ZnO nanoparticle solution.

Al^{3+} doping in ZnO nanocrystals was achieved by the addition of a measured amount of aluminium nitrate nonahydrate, $Al(NO_3)_3 \cdot 9H_2O$, in the precursor solution so that a predetermined [Al]:[Zn] concentration ratio is achieved. In the present work, we controlled the content of Al^{3+} in Zn^{2+} ions in the reaction flask to be 2 and 5 atomic %.

Layer-by-layer film formation on substrate:

To form LbL films of the Ti_3C_2 MXene layer, we first prepared two equal molars (4 mg/mL) of aqueous MXene solutions. One of them is functionalized for a positive charge, $-CH_3^+$ (electrophile) by poly-allylamine hydrochloride and the other is inherently formed nucleophile by surface functional groups (−F, −OH) during exfoliation. The pre-cleaned quartz and ITO substrates were treated with a base piranha solution (NH_4OH: H_2O_2 = 3:1) to deprotonate the

surface. Since the substrate is primarily nucleophilic, we first immersed the substrate into the electrophilic MXene solution for 10 min. To remove excess (physically absorbed) MXene from the surface, the substrates were dipped in two separate deionized water baths for 1 min each. They were then dipped in negatively charged MXene solution for 10 min so that they could attach to the positively charged surface of the preceding layer. The substrates were then washed in deionized water two times. This led to the formation of a bilayer Ti_3C_2 MXene layer on the surface. To form multilayer films of MXene, the dipping procedure was repeated in sequence a desired number of times.

For ZnO nanoparticle LBL films, we followed the same procedure. ZnO nanoparticles are readily formed with hydroxyl termination ion on the surface which served as a negative charge during the LBL process. To form the LBL film, we used 0.5 mM PAH aqueous solutions for a positive charge between two consecutive ZnO nanoparticle layers.

Fabrication of devices:

The formation of a metal-semiconductor junction between the MXene layer and ZnO nanoparticles was a part of the LbL film-deposition procedure which relies on an electrostatic assembly process followed by van der Waals force. Two types of junctions were formed: (1) a junction between the MXene layer with ZnO nanoparticles and (2) a junction in reverse sequence, that is ZnO nanoparticles and MXene layer. Characterization of reverse junctions with the same set of electrodes enabled us to separate the junction characteristics from the effect of the interfaces with the electrodes.[52, 53]

For STM characterization of the metal-semiconductor junction, a monolayer of MXene was formed by dipping the ITO-electrode in an aqueous solution of positively charged MXene followed by negatively charged ZnO nanoparticles. Each dipping was followed by two times washing in water to remove unbound moieties from the surface. To form a multilayer MXene film, the dipping sequence was cycled for a desired number of times using positive and negative charge MXene solutions.

For device fabrication on the ITO substrate, we first grew the MXene layer by LBL technique with desired thickness and then deposited the Al-doped ZnO layer by spin coating. To compare the MXene electrode effect a similar device was fabricated without the MXene layer.

Characterization of heterojunctions through STM studies:

All STM images were recorded at room temperature and ambient conditions. A mechanically cut Pt/Ir tip was used for imaging. All STM images were recorded at a constant current mode with a bias voltage of 0.5 V to 1.2 V and a tunneling current of 0.04 to 0.3 nA. Typically, the

STM displays the average current across the image that deviates from the set-point current and varies from image to image slightly due to an integral part of the feedback loop.

Scanning tunneling spectroscopy (STS) at RT is used to measure the dependence of the tunneling current (I) and the first derivative of the tunneling current (dI/dV) on voltage, which yields information about the electronic structure and bandgap of the MXene nanosheets and ZnO nanoparticles.[54,55] Because dI/dV spectra provide the localized density of states (LDOS) of the surface, such a spectrum may involve a contribution from defects, impurities, surface states, local geometry, local stoichiometry, and so forth. To compensate for this localized nature of STS measurements, I-V characteristics were recorded at many different points on each thin film. For a spectrum, the tip is positioned above the film and the feedback loop is switched off. The bias voltage is then swept over the energy range. The tip approaching tunneling current was kept low (between 0.04 to 0.3 nA) so that the tip did not influence the energy states of the nanocrystals. Since biases are applied to the sample concerning the tip, positive and negative voltage probed the conduction and valance band of the material, respectively. All results presented in the manuscripts are the average of 20 acceptable spectra of a sample.

Characterization:

The as-prepared nanomaterials and nanocomposites were characterized by X-ray diffraction (XRD) patterns, optical absorption spectroscopy (UV-Vis), scanning tunneling microscopy (STM), Scanning Electron Microscopy (FESEM), energy dispersive X-ray (EDX) analysis, transmission electron microscopy (TEM), and high-resolution TEM (HR-TEM). The measurements were carried out with a Shimadzu UV-2550 spectrophotometer, a Rigaku Miniflex 600 powder diffractometer, a Park XE7 AFM, a Zeiss FESEM, and a JEM 2100F JEOL TEM, respectively.

The morphological study of the surface was performed by an XE-7, Park AFM, (Park Systems Corp., South Korea). The topographical investigation was done by STM mode AFM with a Pt-Ir tip having a radius of 20 nm (approx.). All images were obtained at a scan rate of 0.5 Hz under ambient conditions.

To locate the conduction and valence band edges of MXene, and ZnO nanoparticles, the tunneling current of the self-assembled monolayer film of the nanocrystals was recorded with a Park XE7 scanning tunneling microscope (STM) under ambient conditions. The density of states (DOS) of the nanocrystals enabled us to locate the band edges of the semiconductors concerning the Fermi energy. For STM measurements, the voltage was applied to the substrate.

RESULTS AND DISCUSSIONS:

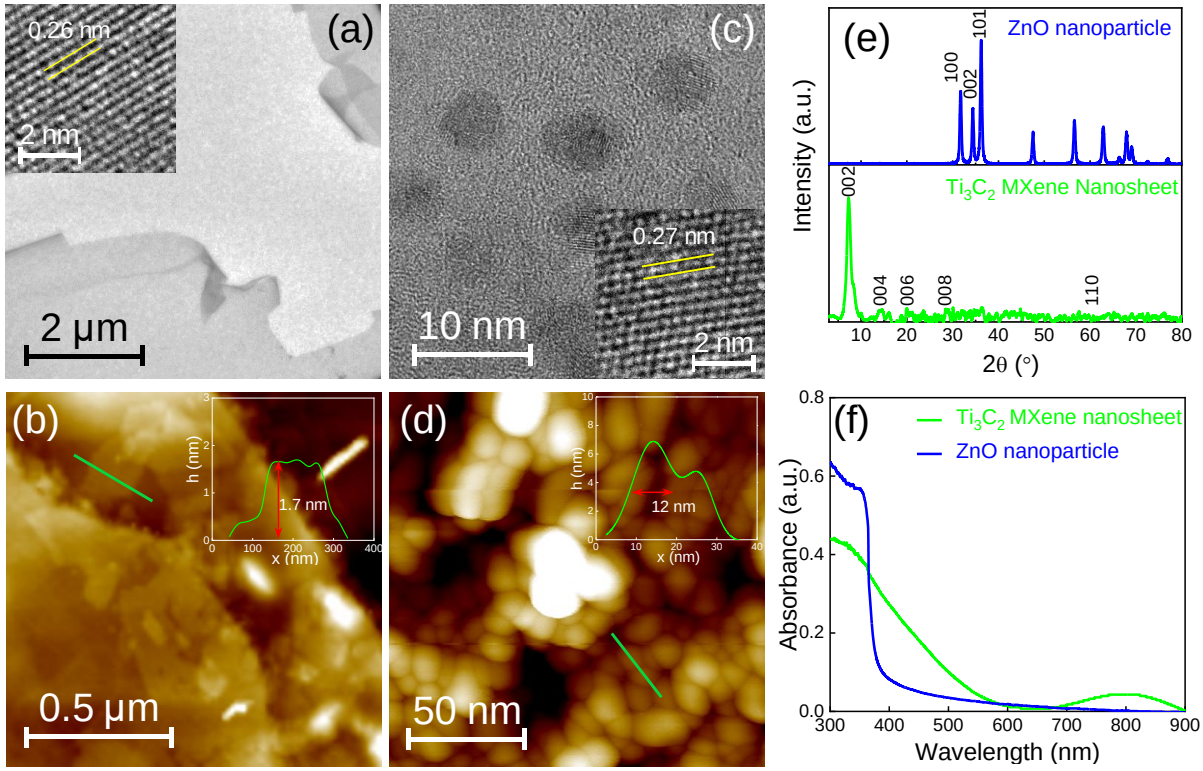

Figure 1: Characterization of the Ti_3C_2 MXene nanosheets and ZnO nanoparticles: (a,c) TEM and HRTEM (inset) image of exfoliated nanosheets (a), and ZnO nanoparticles (c). (b,d) AFM topographical image and line profile (inset) of MXene layer (b), and ZnO nanoparticles (d). (e) XRD spectrum of Ti_3C_2 (green) and ZnO nanoparticle (blue) thin films. (f) UV-Vis spectroscopy of Ti_3C_2 nanosheets (green) and ZnO nanoparticles (blue) in an aqueous solution.

The as-prepared MXene nanosheets show a typical two-dimensional (2D) nanosheet structure, with a size of more than 4 µm as revealed in the TEM image of Figure 1a. A High-resolution (HR) TEM image of the layer in the inset of Figure 1a demonstrates the arrangement of atoms with a lattice constant of 0.26 nm. The single or few-layer MXene nanosheets of 0.8-2.8 nm thickness and 200-800 nm in size were delaminated from these larger nanosheets by short-term ultrasonication. The AFM topographical image of the layers and corresponding line scan of one of the bilayer nanosheets is presented in Figure 1b. The XRD pattern of MXene nanosheets in Figure 1e (green) shows one strongest (002) characteristic diffraction peak at $2\theta = 7.3°$ because only one surface is exposed by X-ray.[56] The structural properties of MXene do not change significantly after being functionalized with PAH as revealed by the XRD, UV-Vis spectra, and AFM images in the Supporting information, Section 1.

The as-synthesized ZnO nanoparticles were also characterized by TEM and HRTEM. The ZnO nanoparticle forms a spherical shape with a diameter of 6-10 nm as demonstrated in Figure 1c. The HRTEM image in the inset confirms the lattice constant of 0.27 nm along the (101) plane which fits well with the XRD spectra in Figure 1e (blue). The AFM image of the ultrathin ZnO nanoparticles film in Figure 1d shows the agglomeration of spherical nanoparticles with a typical diameter of 10-12 nm. Although the size is slightly larger than the TEM image, this may be due to the tip-convolution effect of AFM. The UV-Vis spectroscopy in Figure 1f also confirms the successful synthesis of Ti_3C_2 MXene nanosheets and ZnO nanoparticles dissolved in an aqueous medium. The characterization of Al-doped ZnO nanoparticles is discussed in the Supporting information, Section 2. Since we aim to grow a self-assembled layer-by-layer film of these two materials to form a metal-semiconductor junction, optical absorbance spectroscopy is a very effective method to follow the absorbance peak at a particular wavelength to monitor growth. Here for both ZnO nanoparticles and MXene nanosheets, we followed the absorption at the wavelength of 350 nm.

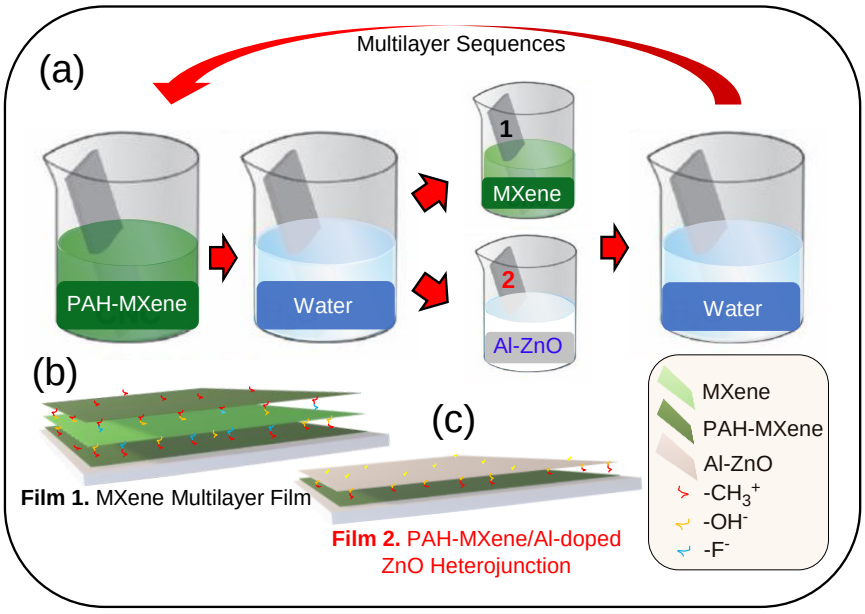

Figure 2. Schematic representation of the layer-by-layer film: (a) Layer-by-layer sequences of the multilayer film of MXene and MXene/Al-ZnO heterojunction. (b) Multilayer MXene film on a quartz substrate. (c) Heterojunction formed between PAH●MXene/Al-doped ZnO monolayer on ITO substrate. Symbols for different components are represented in the legend.

To form MXene-ZnO (metal-semiconductor) junction via a layer-by-layer approach we first ensure the ability of each component to form a stable multilayer film. Figure 2a represents the scheme of the layer-by-layer film formation technique on a solid substrate. After each dipping

cycle, layer formation was confirmed by measuring optical absorption and finally AFM for a scratch profile to determine the multilayer film thickness. A schematic representation of a multilayer MXene film on a quartz substrate and a PAH●MXene/Al-doped ZnO nanoparticle monolayer heterojunction on an ITO substrate is shown in Figure 2b and 2c, respectively.

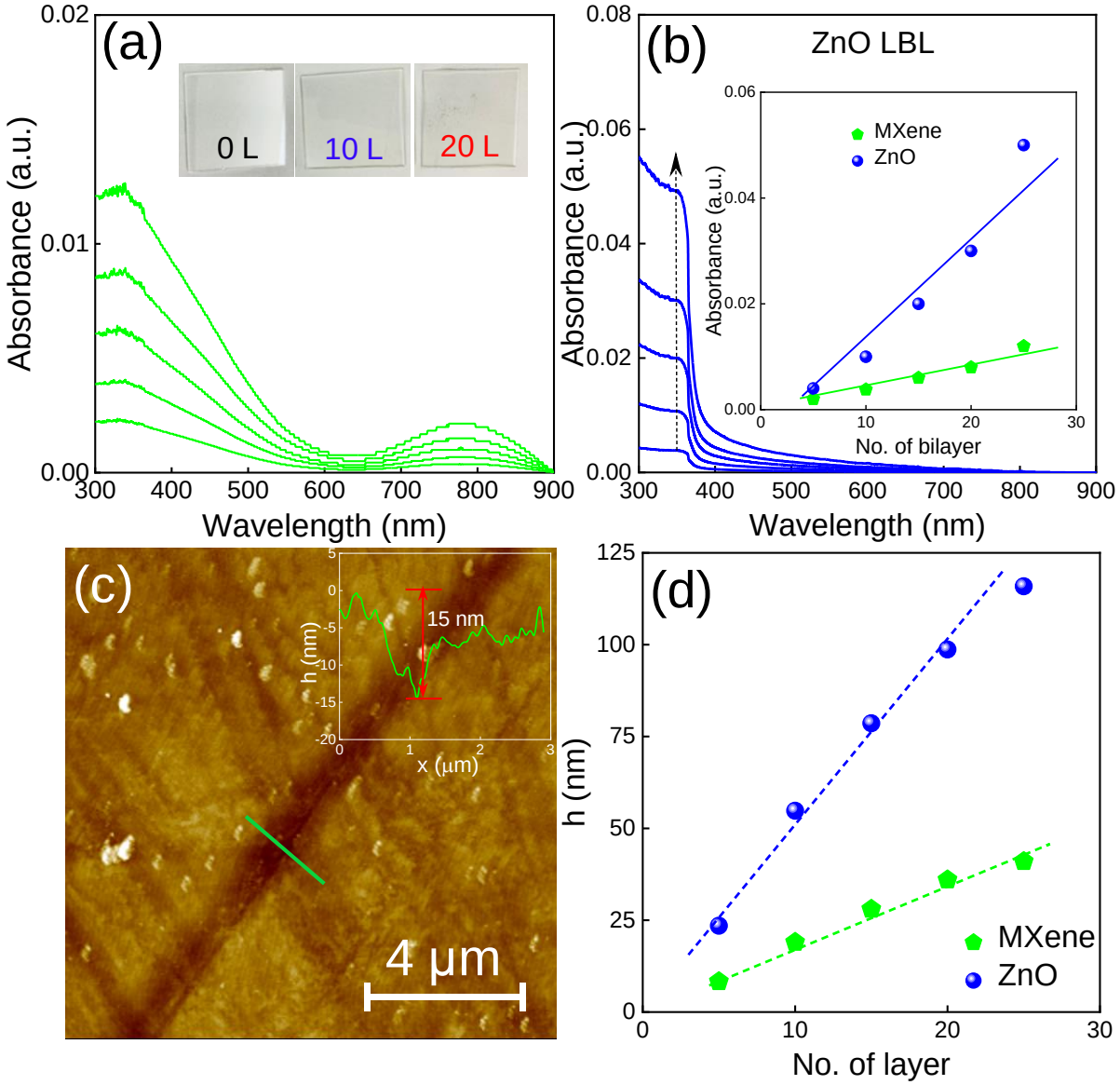

Figure 3: Characterization of the layer-by-layer films on quartz substrate: (a,b) Optical absorbance of Ti_3C_2 multilayer (a), and ZnO nanoparticle layer (b). Photographic images of quartz substrate after sequential multilayer film (inset of a). Absorbance at 350 nm of LbL films versus the number of deposited layers for the films deposited (inset of b). (c) AFM topography and depth profile of a scratch (inset) on a 10 L Ti_3C_2 film. (d) Plots of the thickness of the two films as a function of the number of deposited layers.

In Figure 3a, we show the optical absorption of the MXene film on quartz substrate for a different number of $MXene^{+}/MXene^{-}$ bilayers. The absorption profile of the LbL films matched with the dispersed MXene solution, and grew linearly with the number of layers (inset of Figure 3b (red)). The colour changes of the photographic image in the inset of Figure 3a also confirm the formation of multilayer film through the LBL process. Similarly, the ZnO nanoparticle also grew linearly (Figure 3b). The multi-layered films were further characterized by AFM to measure the roughness and thickness of the film. To measure the thickness from AFM topography, an intentional scratch on the films was made. A typical AFM topography and its corresponding depth profile for a 10-layered MXene film are presented in Figure 3c. Plots of thickness versus the number of layers in Figure 3d imply the linear growth of the layers of MXene nanosheets and ZnO nanoparticle films. The thickness of 25-layered films was 42 nm, implying that each layer corresponds to more than 1 nm in thickness which also suggests that most of the nanosheets are bilayer in nature.

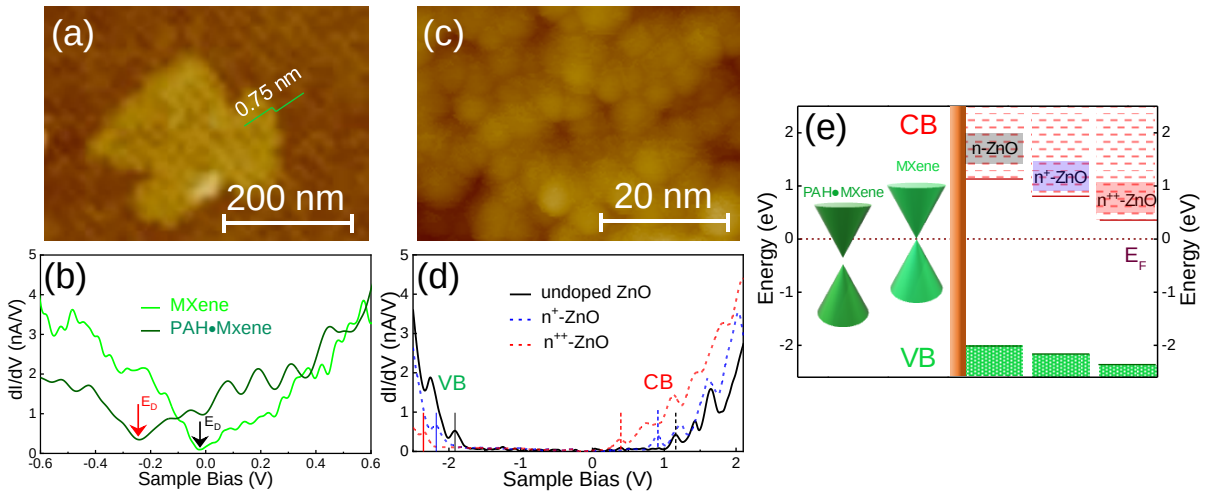

Figure 4: Scanning tunneling spectroscopy of Ti_3C_2 nanosheet and Al-doped ZnO nanoparticles: (a) STM topography and line profile of a Ti_3C_2 monolayer, (b) dI/dV spectra from an average of 10 I-V characteristics at the different spots on the monolayer (green), and PAH functionalized (olive) Ti_3C_2 nanosheet. (c) STM topography of Al-doped ZnO monolayer, (d) dI/dV spectra of the monolayer of n-ZnO (black), n^{+}-ZnO (blue), n^{++}-ZnO (red). VB and CB are marked at negative and positive sample biases, respectively. (e) Energy band positions of individual materials from dI/dV spectra; The broken lines indicate the location of the Fermi level.

After the successful growth of the LBL films, we focussed on their electronic properties by varying thicknesses. We first characterize the MXene nanosheets and the monolayer of ZnO

nanoparticles with a Pt/Ir STM tip. A typical topographic image of a single-layer MXene nanosheet on HOPG and a monolayer of Al-doped ZnO nanoparticles on the ITO substrate is presented in Figures 4a and 4b, respectively. The line profile (inset of Figure 4a) along the line on the layer reveals one atomic layer thickness of Ti_3C_2 MXene. A topographical STM image of the PAH●MXene nanosheet is presented in the Supporting Information, Figure S1d. To know the electronic nature of the material, it is necessary to probe their band gap and energy levels concerning the Fermi level which gives a qualitative idea for the formation of a junction between two materials. Here, we aimed to determine the density of states, conduction, and valance band position of the nanosheets and nanoparticles concerning their Fermi energy through scanning tunneling spectroscopy.

The dI/dV spectra of MXene and PAH functionalized MXene are presented in Figure 4b. In both cases, the local DOS is conducting nature. However, a non-zero differential conductance at 0 V and zero DOS slightly shifted (0.05 eV) from the Fermi level observed in the single-layer MXene, termed Dirac point, E_D of this layer. The dI/dV spectrum of PAH-functionalized MXene revealed an E_D value of -0.24 eV. The shifting of the Fermi level towards the unoccupied region may originate from the amine (NH_2) functionalized Ti_3C_2 which exhibits n-doping due to the electron-donating characteristics of the amine end groups.[46] So, the doping by PAH functionalization lowers the work function of MXene by 0.24 eV, indicating that it may be a promising electrode for electron injection.

The spectrum on the monolayer of undoped ZnO nanoparticles reveals a mild n-type nature with an electronic band gap of 3.25 eV (Figure 4d). The band gap is estimated from the gap between the two rising edges of the dI/dV spectra in positive and negative biases. The increased Al-doping concentrations not only shift the Fermi level towards the conduction band of the ZnO nanoparticles it also reduces the band gap significantly. The shifting of the Fermi level towards CB implies more n-type nature of the ZnO nanoparticles. The band gap becomes reduced to 2.85 eV when doped up to 5% Al in ZnO.

In Figure 4e, we plotted the energy band positions of individual materials. We looked at the DOS spectra for CB and VB band edges concerning the Fermi level at 0 V and plotted them at the energy scale. The cones here are represented to indicate the Dirac point of the MXene monolayers which is placed just above and below the Fermi level. The band alignment between the Al-doped ZnO nanoparticles and the MXene layer evidences a large band offset at the junction by CB of the semiconductor and the Fermi-level of the MXene layer. Only in the case of the PAH●MXene layer, the offsets are reduced which can lower the junction resistance

significantly. This figure, in essence, reflects how doped ZnO semiconductors could form metal-semiconductor junctions with the MXene.

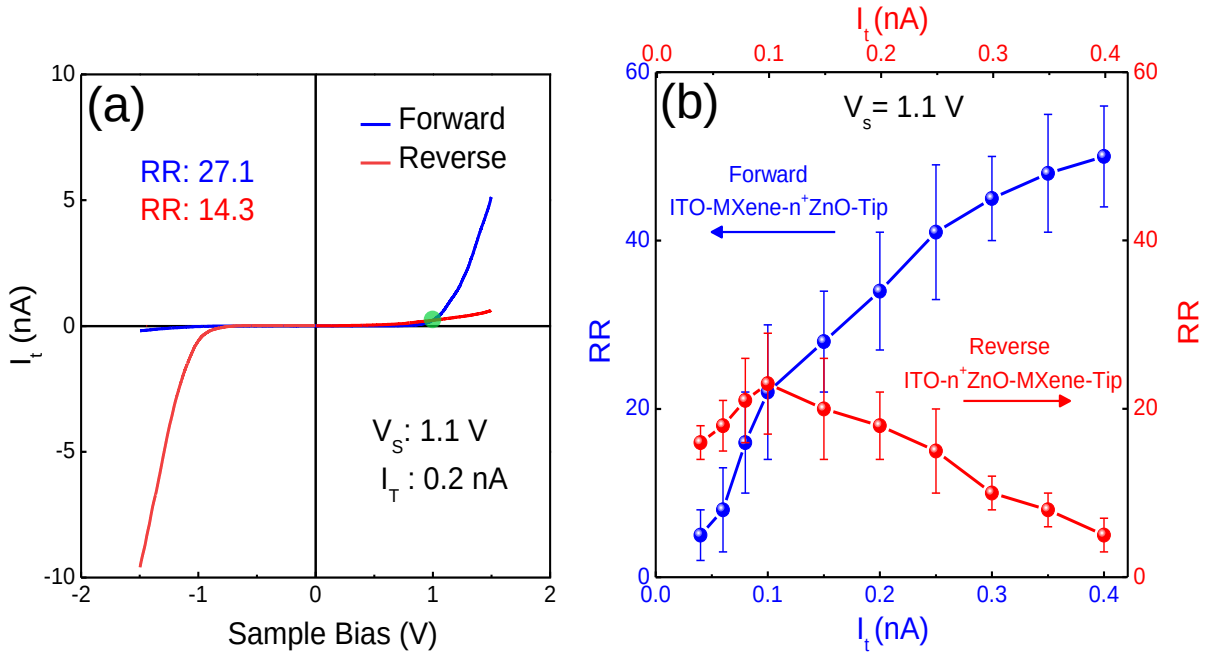

Figure 5: Tip-sample separation dependent characteristics of the MS junction: (a) Current-voltage characteristics of MXene-n^+ ZnO junction on ITO in forward (blue) and reverse (red) sequences. The green dot represents the setpoint during STS spectroscopy. Scanning parameter: V_b=1.1 V, I_t=0.2 nA. (b) The plot of rectification ratio (RR) vs tunneling current (I_t) at a fixed sample bias of 1.1 V.

In characterizing a junction of two materials by STM tip, it is also important to study the reverse sequence, tip-sample separation, and the nature of individual materials to eliminate the influence of tip work function and band bending effects. We hence first characterized the individual materials by STM tip. The I-V characteristics of Ti_3C_2 MXene nanosheets in Figure S3a demonstrate a slight asymmetric due to the work function differences between the Pt/Ir tip and the ITO electrode. The I-V characteristics and corresponding DOS spectra in Figure 3b signify that the MXene exhibits semi-metallic nature. The I-V characteristics of the ultrathin film of undoped and Al-doped ZnO nanoparticles on ITO substrate are demonstrated in Figure S3b. The plots show that all films are semiconductors in nature. Although a large asymmetry arises with the increase of Al doping concentration due to the shifting of the Fermi level towards the CB position. Due to the higher carrier density of doped ZnO nanoparticles, they form a Schottky contact with ITO electrodes. Thus, a rectifying nature is noticeable with the increase in doping concentration.

Although the Al-doped ZnO nanoparticle shows rectification, the rectification ratio is considerably modified after the introduction of the 2D-metal MXene layer as characterized by

the current-voltage characteristics (Figure 5a) in both sequences. This drastic change in the rectification or on-off ratio occurred due to the change in the work function of the metal substrate by the MXene layer. Hence, the rectifying characteristics of the junctions confirm the Schottky junctions in both sequences. Notably, since the direction of rectification is inverted in forward and reverse sequences while keeping the electrode combinations the same, we could infer that the junctions between the MXene-ZnO monolayer indeed rectifying in nature. The rectification ratio (RR) of 2% Al-doped ZnO junctions after introducing the MXene layers in the tunnelling condition of 1.1 V, 0.2 nA is presented in the inset.

As stated earlier, a tip-sample separation measurement was performed to rule out the tip band-bending effect. Since the STM tunneling condition is a crucial factor for controlling the magnitude of current by changing the tip-sample separation (d), a plot of the tunneling current-dependent rectification ratio is revealed in Figure 5b. The decrease of **d** not only enhances the tunneling current due to the increased transmission probability it is also sensitive to the band bending at the tip-sample junction.[18] To abate these effects, we choose an optimal range of tunnelling conditions (V_b = 1.0-1.2 V, I_t = 0.08-0.22 nA) where tip-sample separation did not affect the rectifications much in the MS junction. At a very low tunneling current, the rectification ratio is reduced due to insufficient electron flow through the junctions. The higher rectification ratio in the forward sequence (Figure 5b, blue) is due to the larger current flow in forwarding bias, whereas the current in reverse bias is also increased in the case of reverse sequence (Figure 5b, red), resulting lower in rectification. So, the setpoint was chosen where the rectification ratio plot overlapped in both sequences.

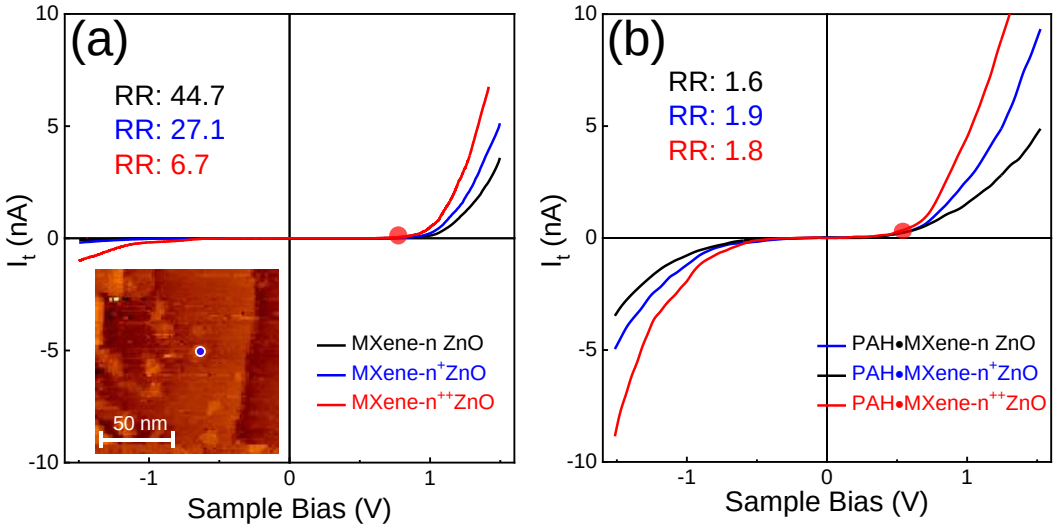

Figure 6: Current-Voltage characteristics of different MS-junctions: (a) ITO-MXene|ZnO-tip junctions. Scanning parameter: V_b=1.1 V, I_t=0.2 nA. (b) ITO-PAH●MXene|ZnO-tip junction. RR and V_{TH} denote the rectification ratio and the threshold voltage of the diode, respectively.

After ruling out junction characteristics issues, we were interested to form MS-junction by varying the doping concentration of the semiconductor. The IV characteristics of different junctions and the rectification ratio are presented in Figure 6a. The rectification ratio is reduced with the increase of doping concentrations. The Schottky barrier width at the junction is reduced with the increase of doping concentration which facilitates electrons to tunnel through the thin barrier, resulting in a higher reverse current and lower rectification ratio. Surprisingly, the rectifying behaviors of all junctions almost disappeared and turned into Ohmic-like ones when a PAH-functionalized MXene was introduced in between the ITO and ZnO layers (Figure 6b). The STS data of the junctions are presented in Supporting Information, Section 4. The non-rectifying junction was distinguishable from the Schottky MS-junction with its asymmetric I-V.

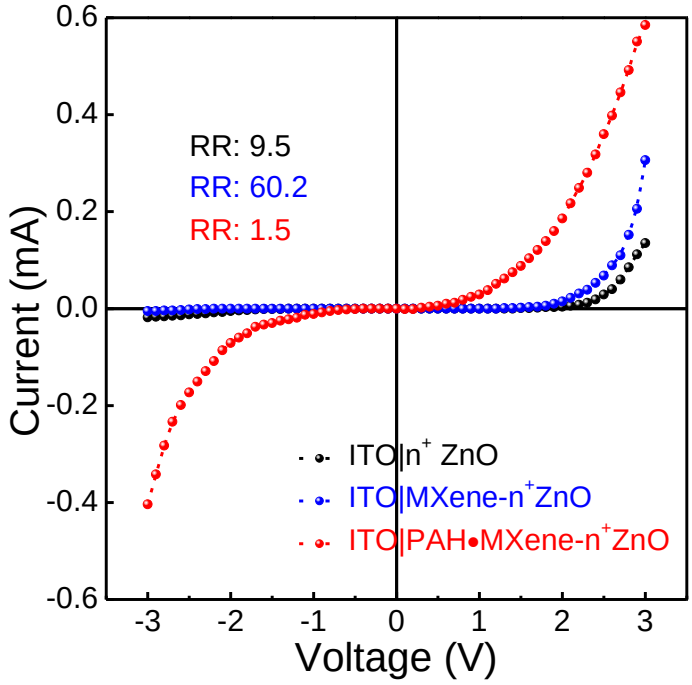

Figure 7: Current-voltage characteristics of MS junction device based on 2% Al-doped ZnO and Ti_3C_2 MXene on ITO substrate.

After analyzing the MXene-based metal-semiconductor junction by STM, we compared the results with fabricating devices, similar to the structure used in the photovoltaic electron transporting layer (ETL). Here the ZnO layer was formed on the ITO substrate and in another structure MXene layer was introduced on the ITO substrate before the ZnO layer formation to realize the 2D-metal effect in MS-junction. The films were characterized by FESEM and XRD to check the morphology and structural change of the composites (Supporting information, Section 5). In Figure 7, both ZnO and MXene-ZnO film on ITO shows rectifying nature and

the rectification ratio (On-Off ratio) is largely enhanced after introducing the MXene layer. Contrastingly the introduction of the PAH●MXene layer between ITO and n^+-ZnO layer reduces the rectification and transforms it into a non-rectifying junction at the interface. To check the stability of the I-V measurements in the PAH●MXene device, we ran several cycles of consecutive measurements. The nature of the I-V and current magnitude does not change significantly suggesting a very stable thin film formation by the PAH functionalized MXene and doped ZnO nanoparticle. The I-V characterization with varying Al-doped ZnO nanoparticles is discussed in the Supporting Information, Section 6. A schematic representation of the possible band alignment is demonstrated in Figure 8.

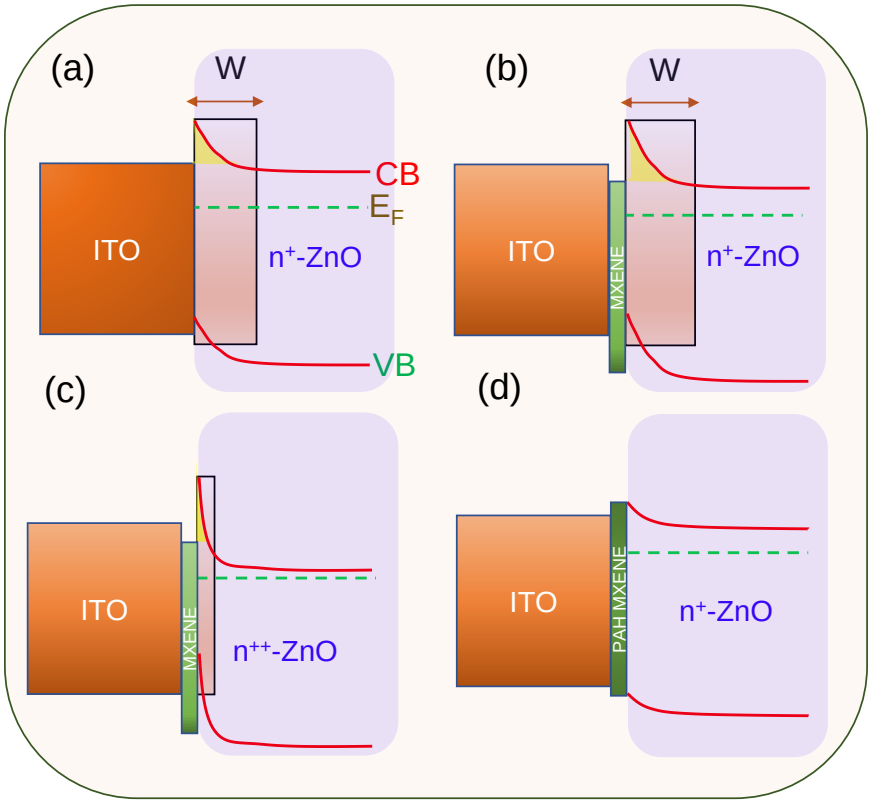

Figure 8: Schematic band diagram of ITO, MXene, PAH●MXene, and Al-doped ZnO junction: (a) Band positions of ITO and n^+-ZnO nanoparticles after contact. CB, VB, and E_F positions are marked. (b) Band diagram of MXene nanosheets and n^+-ZnO nanoparticles after contact. (c) Band diagram of MXene nanosheets and n^{++}-ZnO nanoparticles after contact. (d) Band diagram of PAH functionalized MXene nanosheets and n^+-ZnO nanoparticles after contact. The transparent red shadow region in (a,b,c) is marked as a depletion region of width W. The yellow-shaded region denotes the Schottky barrier height.

The insertion of MXene nanosheet on ITO substrate forms more Schottky barrier by n^+ ZnO nanoparticles as revealed in Figures 8a and 8b due to the high work function of the MXene

layer than ITO substrate. Thus, the modified MS-junction show enhanced rectifying characteristics when probed by the STM tip. In Figure 8c, the Schottky barrier height does not change but the width of the barrier (yellow-shaded region) is reduced due to the high doping of n^{++} ZnO nanoparticles. Owing to the thin barrier, the electron can tunnel through the junction and increases the reverse bias current which reduces the resistance at the junction. The PAH functionalized MXene on the other hand reduces the Schottky barrier and converted it to a non-rectifying band alignment (Figure 8d). The non-rectifying junction supports two main points, (i) the reduced Fermi level pinning by functionalized MXene, and (ii) the work function modulation. While the MXene-ZnO layer shows the Schottky junction, the PAH●MXene-ZnO layer exhibits non-rectifying characteristics. Therefore, the non-rectifying nature of the MS-junction was attributed to the work function modulation of MXene by functionalization which aligns with the semiconductor conduction band and reduced Fermi-level pinning at the MXene-ZnO interface. Sometimes the PAH●MXene-ZnO junctions exhibited a Schottky nature similar to that of the MXene-ZnO junctions. This might have been caused by some part of the MXene consequently not being fully functionalized.

MXene can play a significant role in improving optoelectronic performance by tuning the work function. Here, the suppressing effect of Fermi level pinning in MS junctions by PAH functionalized MXene is studied. A simple chemical approach tunes the work function of MXene and lowers the Schottky barrier height in the ITO-ZnO junction. This work can provide a new strategy for the extensive use of MXene to overcome the negative effects of Fermi-level pinning and provides low-resistance transparent flexible electrodes in optoelectronic devices.

4. CONCLUSIONS:

In conclusion, we have formed a metal-semiconductor junction using Ti_3C_2 MXene nanosheets and Al-doped ZnO nanoparticles on an ITO substrate by a layer-by-layer self-assembly approach. The junctions exhibit Schottky contacts with large resistance at the junctions due to the misalignment of energy between the MXene work function and the conduction band of the ZnO semiconductor. However, the increased doping concentration of the semiconductor reduces the Schottky barrier width which allows electrons to flow in both directions through tunnelling. The PAH-functionalized MXenes, on the other hand, lower the work function of MXene by electron-donating end groups of amines that tend to align with the semiconductor electron affinity levels. As a result, the functionalized MXene and semiconductor junction exhibit non-rectifying behavior with smaller resistance at the junction. This work demonstrates that the MXene interlayer can alter the effective work function of metal between high and low

by functionalization, making it possible to form both rectifying and non-rectifying contacts with a semiconductor on an identical metal electrode. To our knowledge, this work is the first report on metal-semiconductor junction by insertion of MXene layer beyond graphene. Our design strategy with functionalized MXene and doped ZnO nanoparticles can tune the MS junction properties, used for implementing flexible and transparent electrodes for optoelectronic applications. This approach establishes a significant advance toward the fabrication of transparent conductive electrodes in solar cells with low cost, high stability, and flexibility that are essential to replace ITO in photovoltaic devices.

ASSOCIATED CONTENT

Supporting Information.

The Supporting Information is available free of charge at https://pubs.acs.org/doi/*********. Supplementary data for the characterization of PAH●MXene and Al-doped ZnO nanoparticles (Section 1 and Section 2); supplementary STS data of MXene, PAH●MXene and Al-doped ZnO nanoparticles (Section 3); additional STS data of the junctions (Section 4); supplementary data for the characterization of thin film device (Section 5); additional IV data for 5% Al-doped ZnO based device (Section 6). (**PDF**)

AUTHOR INFORMATION

Corresponding Authors

Abhijit Bera: Midnapore College (Autonomous), Midnapore, West Bengal, 721101, India; orcid.org/0000-0003-4898-9797;

Email: abhijit.bera@midnaporecollege.ac.in

Authors

Riya Nag: Midnapore College (Autonomous), Midnapore, West Bengal, 721101, India

Rama Kanta Layek: School of Engineering Science, Department of Separation Science, LUT University, Mukkulankatu 19, FI-15210 Lahti, Finland

Complete contact information is available at: https://pubs.acs.org/10.****/acsanm.*******

Author Contributions

AB designed the project. RN synthesized and functionalized the MXene with the help of RKL, AB and RN performed the STM measurements. RN fabricate and characterize the device. AB analyzed the data and wrote the article.

Notes

The authors declare no competing financial interest.

ACKNOWLEDGMENT

This work was supported by the SERB, India grant under file no. EEQ/2020/000156. RN acknowledges SERB for funding the project fellowship. AB acknowledges DST, and Midnapore College Chemistry department for XRD, and optical measurement facilities, respectively.

REFERENCES:

1. Magliulo, M.; Mulla, M. Y.; Singh, M. M.; Macchia, E.; Tiwari, A. K.; Torsi, L.; Manoli, K., Printable, and Flexible Electronics: From TFTs to Bioelectronic Devices. *J. Mater. Chem. C* **2015,** *3*, 12347-12363.

2. Lu, H.; Ren, X.; Ouyang, D.; Choy, W. C. H., Emerging Novel Metal Electrodes for Photovoltaic Applications. *Small* **2018,** *14*, 1703140.

3. Dai, C.; Sun, G.; Hu, L.; Xiao, Y.; Zhang, Z.; Qu, L., Recent Progress in Graphene-Based Electrodes for Flexible Batteries. *InfoMat* **2020,** *2*, 509-526.

4. Cheng, T.; Zhang, Y.; Lai, W.-Y.; Huang, W., Stretchable Thin-Film Electrodes for Flexible Electronics with High Deformability and Stretchability. *Adv. Mater.* **2015,** *27*, 3349-3376.

5. Bae, S.; Kim, H. K.; Lee, Y.; Xu, X.; Park, J.-S.; Zheng, Y.; Balakrishnan, J.; Lei, T.; Kim, H. R.; Song, Y. I.; Kim, Y.-J.; Kim, K. S.; Özyilmaz, B.; Ahn, J.-H.; Hong, B. H.; Iijima, S., Roll-to-Roll Production of 30-inch Graphene Films for Transparent Electrodes. *Nat. Nanotechnol.* **2010,** *5*, 574-578.

6. Tang, H.; Hu, Q.; Zheng, M.; Chi, Y.; Qin, X.; Pang, H.; Xu, Q., MXene-2D layered electrode materials for energy storage. *Prog. Nat. Sci.* **2018,** *28*, 133-147.

7. Ouyang, W.; Chen, J.; He, J.-H.; Fang, X., Improved Photoelectric Performance of UV Photodetector Based on ZnO Nanoparticle-Decorated BiOCl Nanosheet Arrays onto PDMS Substrate: The Heterojunction and $Ti_3C_2T_x$ MXene Conduction Layer. *Adv. Electron. Mater.* **2020,** *6*, 2000168.

8. Feng, S.; Wang, X.; Wang, M.; Bai, C.; Cao, S.; Kong, D., Crumpled MXene Electrodes for Ultra-stretchable and High-Area Capacitance Supercapacitors. *Nano Lett.* **2021,** *21*, 7561-7568.

9. Yang, L.; Dall'Agnese, C.; Dall'Agnese, Y.; Chen, G.; Gao, Y.; Sanehira, Y.; Jena, A. K.; Wang, X.-F.; Gogotsi, Y.; Miyasaka, T., Surface-Modified Metallic $Ti_3C_2T_x$ MXene as Electron Transport Layer for Planar Heterojunction Perovskite Solar Cells. *Adv. Func. Mater.* **2019,** *29*, 1905694.

10. Lyu, B.; Kim, M.; Jing, H.; Kang, J.; Qian, C.; Lee, S.; Cho, J. H., Large-Area MXene Electrode Array for Flexible Electronics. *ACS Nano* **2019,** *13*, 11392-11400.

11. Chen, J.; Li, Z.; Ni, F.; Ouyang, W.; Fang, X., Bio-Inspired Transparent MXene Electrodes for Flexible UV Photodetectors. *Mater. Horiz.* **2020,** *7*, 1828-1833.

12. Yan, T.; Li, Z.; Cao, F.; Chen, J.; Wu, L.; Fang, X., An All-Organic Self-Powered Photodetector with Ultraflexible Dual-Polarity Output for Biosignal Detection. *Adv. Mater.* **2022,** *34*, 2201303.

13. Sinha, D.; Lee, J. U., Ideal Graphene/Silicon Schottky Junction Diodes. *Nano Lett.* **2014,** *14*, 4660-4664.

14. Liu, S.; Liao, Q.; Lu, S.; Zhang, Z.; Zhang, G.; Zhang, Y., Strain Modulation in Graphene/ZnO Nanorod Film Schottky Junction for Enhanced Photosensing Performance. *Adv. Funct. Mater.* **2016,** *26*, 1347-1353.

15. Petta, J. R.; Johnson, A. C.; Taylor, J. M.; Laird, E. A.; Yacoby, A.; Lukin, M. D.; Marcus, C. M.; Hanson, M. P.; Gossard, A. C., Coherent Manipulation of Coupled Electron Spins in Semiconductor Quantum Dots. *Science* **2005,** *309*, 2180-2184.

16. Javey, A.; Guo, J.; Wang, Q.; Lundstrom, M.; Dai, H., Ballistic Carbon Nanotube Field-Effect Transistors. *Nature* **2003,** *424*, 654-657.

17. Nishimura, T.; Kita, K.; Toriumi, A., Evidence for Strong Fermi-Level Pinning due to Metal-Induced Gap States at Metal/Germanium Interface. *Appl. Phys. Lett.* **2007,** *91*, 123123.

18. Bell, L. D.; Kaiser, W. J.; Hecht, M. H.; Grunthaner, F. J., Direct Control and Characterization of a Schottky Barrier by Scanning Tunneling Microscopy. *App. Phys. Lett.* **1988,** *52*, 278-280.

19. Tung, R. T.; Kronik, L., Fermi Level Pinning for Zinc-Blende Semiconductors Explained with Interface Bonds. *Phys. Rev. B* **2021,** *103*, 085301.

20. Zhou, L.-X.; Ren, Y.-T.; Chen, Y.-T.; Lv, X.-H.; Jin, C.-D.; Zhang, H.; Gong, P.-L.; Lian, R.-Q.; Wang, R.-N.; Wang, J.-L.; Shi, X.-Q., Quasi-Bonding-Induced Gap States in Metal/Two-Dimensional Semiconductor Junctions: Route for Schottky barrier Height Reduction. *Phys. Rev. B* **2022,** *105*, 224105

21. Chuang, Y.; Liu, C.-Y.; Kao, H.-S.; Tien, K.-Y.; Luo, G.-L.; Li, J.-Y., Schottky Barrier Height Modulation of Metal/n-GeSn Contacts Featuring Low Contact Resistivity by in Situ Chemical Vapor Deposition Doping and NiGeSn Alloy Formation. *ACS Appl. Electron. Mater.* **2021,** *3*, 1334-1340.

22. Murali, K.; Dandu, M.; Watanabe, K.; Taniguchi, T.; Majumdar, K., Accurate Extraction of Schottky Barrier Height and Universality of Fermi Level De-Pinning of van der Waals Contacts. *Adv. Func. Mater.* **2021,** *31*, 2010513.

23. Shen, P.-C.; Su, C.; Lin, Y.; Chou, A.-S.; Cheng, C.-C.; Park, J.-H.; Chiu, M.-H.; Lu, A.-Y.; Tang, H.-L.; Tavakoli, M. M.; Pitner, G.; Ji, X.; Cai, Z.; Mao, N.; Wang, J.; Tung, V.; Li, J.; Bokor, J.; Zettl, A.; Wu, C.-I.; Palacios, T.; Li, L.-J.; Kong, J., Ultralow Contact Resistance between Semimetal and Monolayer Semiconductors. *Nature* **2021,** *593*, 211-217.

24. Zhang, P.; Di, B.; Lei, W.; Wen, X.; Zhang, Y.; Li, L.; Yang, L.; Chang, H.; Zhang, W., Reduced Schottky Barrier Height at Metal/CVD-Grown $MoTe_2$ Interface. *Appl. Phys. Lett.* **2022,** *120*, 261901.

25. Wei, Y.-N.; Hu, X.-G.; Zhang, J.-W.; Tong, B.; Du, J.-H.; Liu, C.; Sun, D.-M.; Liu, C., Fermi-Level Depinning in Metal/Ge Junctions by Inserting a Carbon Nanotube Layer. *Small* **2022,** *18*, 2201840.

26. Yoon, H. H.; Song, W.; Jung, S.; Kim, J.; Mo, K.; Choi, G.; Jeong, H. Y.; Lee, J. H.; Park, K., Negative Fermi-Level Pinning Effect of Metal/n-GaAs(001) Junction Induced by a Graphene Interlayer. *ACS Appl. Mater. Interfaces* **2019,** *11*, 47182-47189.

27. Liu, Y.; Stradins, P.; Wei, S.-H., Van der Waals Metal-Semiconductor Junction: Weak Fermi Level Pinning Enables Effective Tuning of Schottky Barrier. *Sci. Adv.* **2016,** *2*, 1-6.

28. Byun, K.-Y.; Chung, H.-J.; Lee, J.; Yang, H.; Song, H. J.; Heo, J.; Seo, D. H.; Park, S.; Hwang, S. W.; Yoo, I.; Kim, K., Graphene for True Ohmic Contact at Metal−Semiconductor Junctions. *Nano Lett.* **2013,** *13*, 4001-4005.

29. Giovannetti, G.; Khomyakov, P. A.; Brocks, G.; Karpan, V. M.; van den Brink, J.; Kelly, P. J., Doping Graphene with Metal Contacts. *Phys. Rev. Lett.* **2008,** *101*, 026803.

30. Georgakilas, V.; Otyepka, M.; Bourlinos, A. B.; Chandra, V.; Kim, N.; Kemp, K. C.; Hobza, P.; Zboril, R.; Kim, K. S., Functionalization of Graphene: Covalent and Non-Covalent Approaches, Derivatives and Applications. *Chem. Rev.* **2012,** *112*, 6156-6214.

31. Ma, X.; Mi, Y.; Zhang, F.; An, Q.; Zhang, M.; Hu, Z.; Liu, X.; Zhang, J.; Tang, W., Efficient Ternary Polymer Solar Cells with Two Well-Compatible Donors and One Ultranarrow Bandgap Nonfullerene Acceptor. *Adv. Energy Mater.* **2018,** *8*, 1702854.

32. Li, Y.; Yu, H. Y.; Li, J.; Wong, S.-M.; Sun, X. W.; Li, X.; Cheng, C.; Fan, H. J.; Wang, J.; Singh, N.; Lo, P. G.-D.; Kwong, D.-L., Novel Silicon Nanohemisphere-Array Solar Cells with Enhanced Performance. *Small* **2011,** *7*, 3138-3143.

33. Etgar, L.; Gao, P.; Xue, Z.; Peng, Q.; Chandiran, A. K.; Liu, B.; Nazeeruddin, M. K.; Grätzel, M., Mesoscopic $CH_3NH_3PbI_3/TiO_2$ Heterojunction Solar Cells. *J. Am. Chem. Soc.* **2012,** *134*, 17396-17399.

34. Dong, H.; Wu, Z.; Xi, J.; Xu, X.; Zuo, L.; Lei, T.; Zhao, X.; Zhang, L.; Hou, X.; Jen, A. K.-Y., Pseudohalide-Induced Recrystallization Engineering for $CH_3NH_3PbI_3$ Film and Its Application in Highly Efficient Inverted Planar Heterojunction Perovskite Solar Cells. *Adv. Energy Mater.* **2017,** *28*, 1704836.

35. Zhao, X.; Liu, S.; Zhang, H.; Chang, S.-Y.; Huang, W.; Zhu, B.; Shen, Y.; Shen, C.; Wang, D.; Yang, Y.; Wang, W., 20% Efficient Perovskite Solar Cells with 2D Electron Transporting Layer. *Adv. Func. Mater.* **2018,** *29*, 1805168.

36. Jiang, Q.; Zhang, X.; You, J., SnO2: A Wonderful Electron Transport Layer for Perovskite Solar Cells. *Small* **2018,** *14*, 1801154.

37. Noh, M. F. M.; Teh, C. H.; Daik, R.; Lim, E. L.; Yap, C. C.; Ibrahim, M. A.; Ludin, N. A.; Yusoff, A. R. b. M.; Jang, J.; Teridi, M. A. M., The architecture of the electron transport layer for a perovskite solar cell. *J. Mater. Chem. C,* **2018,** *6*, 682-712.

38. Chatterjee, S.; Pal, A. J., Introducing Cu_2O Thin Films as a Hole-Transport Layer in Efficient Planar Perovskite Solar Cell Structures. *J. Phys. Chem. C* **2016,** *120*, 1428-1437.

39. Zhao, D.; Sexton, M.; Park, H.-Y.; Baure, G.; Nino, J. C.; So, F., High-Efficiency Solution-Processed Planar Perovskite Solar Cells with a Polymer Hole Transport Layer. *Adv. Energy Mater.* **2015,** *5*, 1401855.

40. Wang, F.; Endo, M.; Mouri, S.; Miyauchi, Y.; Ohno, Y.; Wakamiya, A.; Murata, Y.; Matsuda, K., Highly Stable Perovskite Solar Cells with an All-Carbon Hole Transport Layer. *Nanoscale* **2016,** *8*, 11882-11888.

41. Guo, Z.; Gao, L.; Xu, Z.; Teo, S.; Zhang, C.; Kamata, Y.; Hayase, S.; Ma, T., High Electrical Conductivity 2D MXene Serves as Additive of Perovskite for Efficient Solar Cells. *Small* **2018,** *14*, 1802738.

42. Agresti, A.; Pazniak, A.; Pescetelli, S.; Di Vito, A.; Rossi, D.; Pecchia, A.; Auf der Maur, M.; Liedl, A.; Larciprete, R.; Kuznetsov, D. V.; Saranin, D.; Carlo, A. D., Titanium-Carbide MXenes for Work Function and Interface Engineering in Perovskite Solar Cells. *Nat. Mater.* **2019,** *18*, 1228-1234.

43. Chen, X.; Xu, W.; Ding, N.; Ji, Y.; Pan, G.; Zhu, J.; Zhou, D.; Wu, Y.; Chen, C.; Song, H., Dual Interfacial Modification Engineering with 2D MXene Quantum Dots and Copper Sulphide Nanocrystals Enabled High-Performance Perovskite Solar Cells. *Adv. Func. Mater.* **2020,** *30*, 2003295.

44. Zhang, J.; Kong, N.; Uzun, S.; Levitt, A.; Seyedin, S.; Lynch, P. A.; Qin, S.; Han, M.; Yang, W.; Liu, J.; Wang, X.; Gogotsi, Y.; Razal, J. M., Scalable Manufacturing of Free-Standing, Strong $Ti_3C_2T_x$ MXene Films with Outstanding Conductivity. *Adv. Mater.* **2020,** *32*, 2001093.

45. Yu, Z.; Feng, W.; Lu, W.; Li, B.; Yao, H.; Zeng, K.; Ouyang, J., MXenes with Tunable Work Functions and Their Application as Electron- and Hole-Transport Materials of Non-Fullerene Organic Solar Cells. *J. Mater. Chem. A*, **2019,** *7*, 11160-11169.

46. Chen, R.-S.; Ding, G.; Feng, Z.; Zhang, S.-R.; Mo, W.-A.; Han, S.-T.; Zhou, Y., MoS2 Transistor with Weak Fermi Level Pinning via MXene Contacts. *Adv. Funct. Mater.* **2022**, 2204288.

47. Chen, J.; Liu, X.; Li, Z.; Cao, F.; Lu, X.; Fang, X., Work-Function-Tunable MXenes Electrodes to Optimize p-$CsCu_2I_3$/n-$Ca_2Nb_{3-x}Ta_xO_{10}$ Junction Photodetectors for Image Sensing and Logic Electronics. *Adv. Func. Mater.* **2022,** *32*, 2201066.

48. Saeed, M. A.; Shahzad, A.; Rasool, K.; Mateen, F.; Oh, J.-M.; Shim, J. W., 2D MXene: A Potential Candidate for Photovoltaic Cells? A Critical Review. *Adv. Sci.* **2022,** *9*, 2104743.

49. Park, J.; Jo, S. B.; Yu, Y.-J.; Kim, Y.; Yang, J. W.; Lee, W. H.; Kim, H. H.; Hong, B. H.; Kim, P.; Cho, K.; Kim, K. S., Single-Gate Bandgap Opening of Bilayer Graphene by Dual Molecular Doping. *Adv. Mater.* **2012,** *24*, 407-411.

50. Alhabeb, M.; Maleski, K.; Anasori, B.; Lelyukh, P.; Clark, L.; Sin, S.; Gogotsi, Y., Guidelines for Synthesis and Processing of Two-Dimensional Titanium Carbide ($Ti_3C_2T_x$ MXene). *Chem. Mater.* **2017,** *29*, 7633-7644.

51. Liu, D.; Kelly, T. L., Perovskite Solar Cells with a Planar Heterojunction Structure Prepared using Room-Temperature Solution Processing Techniques. *Nat. Photon.* **2013,** *8*, 133-138.

52. Bera, A.; Pal, A. J., Molecular Rectifiers based on Donor/Acceptor Assemblies: Effect of Orientation of the Components' Magnetic Moments. *Nanoscale* **2013,** *5*, 518-6524.

53. Bera, A.; Pal, A. J., Aligned Magnetic Domains in p- and n-Type Ferromagnetic Nanocrystals and in pn-Junction Nanodiodes. *ACS Appl. Mater. Interfaces* **2013,** *5*, 12083-12088.

54. Banin, U.; Cao, Y. W.; Katz, D.; Millo, O., Identification of Atomic-Like Electronic States in Indium Arsenide Nanocrystal Quantum Dots. *Nature* **1999,** *400*, 542-544.

55. Bera, A.; Dey, S.; Pal, A. J., Band Mapping Across a pn-Junction in a Nanorod by Scanning Tunneling Microscopy. *Nano Lett.* **2014,** *14*, 2000-2005.

56. Huang, X.; Wu, P., A Facile, High-Yield, and Freeze-and-Thaw-Assisted Approach to Fabricate MXene with Plentiful Wrinkles and Its Application in On-Chip Micro-Supercapacitors. *Adv. Funct. Mater.* **2020,** *30,* 1910048.

TOC Graphic